communications physics

A Nature Portfolio journal

Article

https://doi.org/10.1038/s42005-025-02469-4

Determination of coupling state within a spin-torque oscillator using injection locking

Yuji Nakagawa [1] ✉, Hirofumi Suto [2], Yuya Sakuraba [2] & Tomoyuki Maeda [1]

Dynamic interactions between magnetizations enable complex operations in spintronic devices, such as coupled oscillation in spin-torque oscillators (STOs). Here, we report the experimental determination of coupling states in an STO using an analysis method based on injection locking. The STO is developed for assisted magnetic recording in hard disk drives and exhibits coupled oscillation of two magnetic layers and oscillation of a single magnetic layer depending on bias current polarities, with the former operation improving recording performance. While conventional spectrum measurements yield similar peaks for both oscillations, our method clearly distinguishes between the coupled and single oscillation modes through resistance measurements because of the insensitivity of the coupled oscillation to injection locking, as supported by simulations. Our results demonstrate that the injection locking method provides a sensitive probe for examining coupled oscillation states and is widely applicable to the development of spintronic devices functionalized through dynamic coupling.

Nano-magnets integrated into spintronic devices interact with each other through various mechanisms, including spin-polarized currents, spin waves, and stray fields[1–6]. While these interactions sometimes pose challenges for device integration, as seen in the increased error rates in dense memory cells of magnetoresistive random access memory (MRAM)[5], they can also deliver higher performance and new functionality in other devices, such as spin-torque oscillators (STOs)[1–4,6].

In STOs, spin-polarized currents provide spin-transfer torque (STT) and induce auto-oscillating precession in oscillation layers. The interactions and subsequent coupling between these layers can lead to increased power and improved coherency for microwave signal generator functions[1–3,6–11], as well as focused field distribution for microwave magnetic field emitter functions[4,12–15]. Coupling phenomena also play important roles in recently proposed neuromorphic computing applications[3,16–21]. However, investigating the details of such coupling has been hindered by the nanometer-scale device size and the gigahertz-range oscillation frequency. In previous studies, analysis of coupling states has mainly relied on simulations[9–14] and spectrum measurements, where multiple oscillation peaks arising from different STOs combine as the operation bias changes, suggesting coupled oscillations[1–3].

Another notable phenomenon exhibited by STOs is injection locking[3,19,22–27]. Due to their inherent non-linearity, STO oscillation can be synchronized with an external microwave input, such as a microwave magnetic field or a microwave electrical signal, when the input power is sufficient, and the input frequency is close to the STO oscillation frequency. Injection locking has been studied in terms of improving oscillation characteristics, such as increased output power and reduced phase noise. Furthermore, a method for analyzing STOs based on injection locking has been proposed and demonstrated recently[27], in which the DC resistance change of the STO is monitored during locking to an external microwave magnetic field. Because the oscillation frequency in an STO is related to the oscillation angle of the magnetization, frequency modification by injection locking changes the average angle between the oscillation layers and adjacent layers, resulting in resistance change through the giant magnetoresistance (GMR) effect. This method has several advantages over spectrum measurement, such as classification of actual and fictitious oscillation signals.

The STO analyzed in this study is designed for microwave-assisted magnetic recording (MAMR), which is one of the next key technologies in hard disk drives (HDDs)[13,28]. In this application, the STO is fabricated at the tip of the writer part of the HDD head. Oscillation layers, referred to as field-generation layers (FGLs), emit a stray field as a microwave magnetic field at a frequency of a few tens of GHz. This microwave field, through ferromagnetic resonance excitation of the media magnetization, assists the recording process, in which the recording field from the writer part switches the media magnetizations to the desired direction. Implementation of MAMR has

[1]Corporate Laboratory, Toshiba Corporation, Kawasaki, Japan. [2]Research Center for Magnetic and Spintronic Materials, National Institute for Materials Science (NIMS), Tsukuba, Japan. ✉e-mail: yuji.nakagawa.d94@mail.toshiba

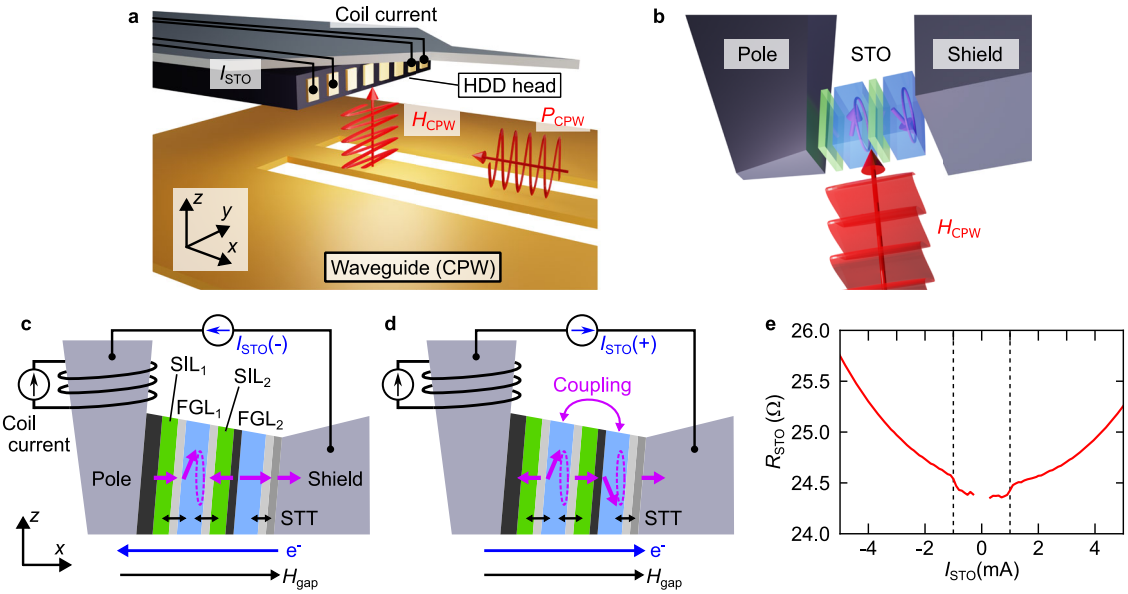

Fig. 1 | Schematic of measurement and STO operations. a Hard disk drive (HDD) head supported by a metal arm and placed on a coplanar waveguide (CPW). The spin-torque oscillator (STO) current (I_{STO}) and coil current are applied through HDD leads on the metal arm and electrodes on the side of the HDD head. A microwave signal applied to the CPW with a power of P_{CPW} generates a microwave magnetic field (H_{CPW}). H_{CPW} is injected into the writer part, which is located near the edge of the HDD head. **b** Magnified view of the writer part. An STO with two spin-injection layers (SILs) and two field-generation layers (FGLs) is fabricated between the pole and shield. The STO width is 45 nm. **c**, **d** Expected STO operations with negative and positive I_{STO}, respectively. SIL$_1$ (Py), FGL$_1$ (FeCo), SIL$_2$ (Py), and FGL$_2$ (FeCo) are separated by Cu spacers (light gray) or spin sinks (dark gray). The Cu spacers enable spin-transfer torque (STT) interaction between the magnetizations (purple arrows) of adjacent layers. The coil current magnetizes the pole, and the magnetic field from the pole (H_{gap}) is applied to the STO. With negative I_{STO}, only FGL$_1$ exhibits oscillation (**c**), while with positive I_{STO}, both FGL$_1$ and FGL$_2$ oscillate with antiparallel coupling (**d**). **e** STO resistance (R_{STO}) as a function of I_{STO}. The steps on the negative and positive sides correspond to SIL$_2$ and SIL$_1$ magnetization reversal, respectively. The vertical dashed lines indicate the I_{STO} values where dR_{STO}/dI_{STO} exhibits peaks.

partly started[14,15,29], and thus STOs have become the second practical spintronic device to be used in HDDs, following the magnetoresistive sensors used in the reader part for decades[30].

Recently, STO structures with two FGLs have been proposed for MAMR, referred to as dual-FGL STO[4,12,14]. During oscillation of this type of STO, the two FGLs are designed to establish an antiferromagnetic configuration through dipolar coupling. Coupled oscillation of FGLs generates a focused field distribution desirable for improving recording performance, and more than 20% increase in recording areal density is expected[4]. However, conventional spectrum measurements have not revealed any distinctive features indicating coupled oscillation in dual-FGL STOs fabricated in HDD heads[14]. Agreement between observed spectrum peaks and micromagnetic simulations has only indirectly suggested coupled oscillation[14]. Therefore, an alternative method for characterizing the oscillation states is needed.

In this study, we demonstrate the determination of the coupled oscillation state in a dual-FGL STO by utilizing injection locking. As shown in Fig. 1a, b, the STO is fabricated in a state-of-the-art MAMR head, and the head is placed on a coplanar waveguide (CPW), which generates an external microwave field for injection locking. Firstly, we found the STO also operates in the opposite bias current direction, in which only one FGL oscillates without coupling. This uncoupled oscillation cannot be distinguished from the coupled oscillation by conventional spectrum measurements because similar oscillation peaks are observed for both bias current polarities. In contrast, we observed an unambiguous difference in injection locking whereby the resistance change appears only for the uncoupled oscillation because the sensitivity to the microwave field differs significantly between the two oscillation states. The absence of the injection locking effect is attributed to Zeeman energy cancellation in the antiparallel configuration. The proposed analysis method provides evidence of the coupled oscillation, a key factor for higher MAMR performance.

Structure and operation of HDD head equipped with STO

Figure 1c, d shows the structure of the writer part of an HDD head. The basic structure consists of a coil, a recording pole, and a shield. The coil current polarity reflects the information to be recorded (0 or 1) and determines the direction of the pole magnetization (up or down). The pole is made of high saturation magnetization materials, such as FeCo-alloy, and its magnetic field transcribes the information onto perpendicularly magnetized grains fabricated on the disk. The typical pole width at the tip (y-direction in Fig. 1c) and write gap (the gap between the pole and shield) are 50 nm and 30 nm, respectively. The shield absorbs the magnetic field emanating from the side wall of the pole (H_{gap}) to enable fine recording. The value of $\mu_0 H_{gap}$ is typically 1.5 T [14].

The STO was fabricated in the write gap for MAMR[14] by depositing the following four types of layers on the side wall of the pole: FGL (5-nm-thick FeCo-alloy), spin-injection layer (SIL) (2-nm-thick Py), spin sink, and Cu spacer, in the following order: spin sink/SIL$_1$/Cu/FGL$_1$/Cu/SIL$_2$/spin sink/FGL$_2$/Cu. The oscillation of FGL magnetization, which generates a microwave magnetic field, is driven by STT from spin-polarized electrons injected from the SILs and the shield through the Cu spacers. The spin sink layers include heavy metals like Ta with short spin-diffusion lengths to block spin injection at the interface. The fabricated STO has a lateral dimension of 45 nm in both y- and z-directions.

The STO operates in two distinct modes depending on the polarity of the bias current (I_{STO}), which is applied to the STO through the pole and shield (Fig. 1c, d). The main mode of operation for MAMR uses positive I_{STO} (Fig. 1d)[14]. Starting from the initial state, where all magnetizations are aligned with the H_{gap} direction, the SIL$_1$ magnetization flips due to STT from the reflected spins at the FGL$_1$ interface. This operation is analogous to that in STT-MRAM, where the magnetization of the recording layer is switched to the antiparallel state relative to the reference layer magnetization[31,32]. After the SIL$_1$ reversal, STT from both the transmitted

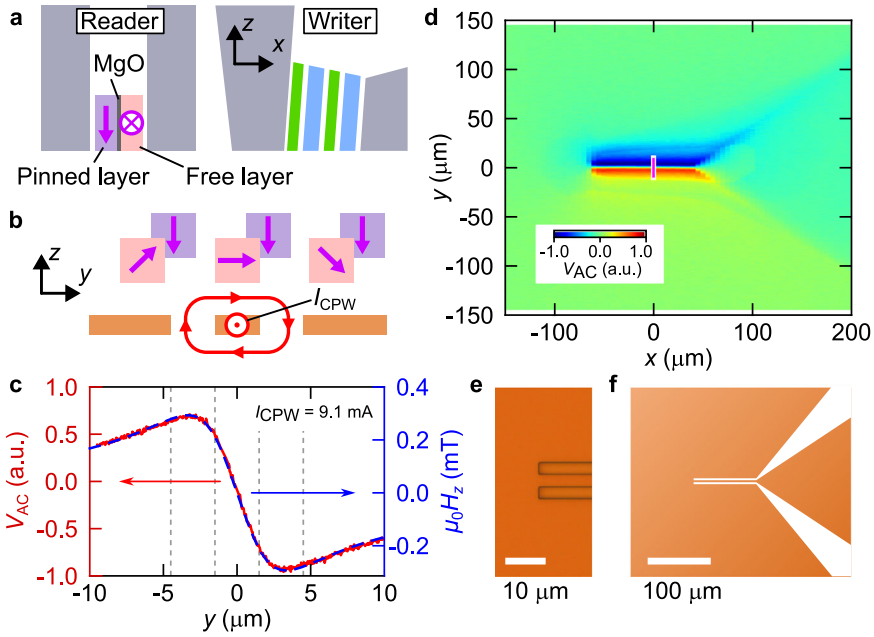

Fig. 2 | Alignment of the HDD head and CPW. **a** Schematic of the reader part in the hard disk drive (HDD) head, fabricated close to the writer part. The tunneling magnetoresistance (TMR) reader consists of an MgO barrier, a pinned layer, and a free layer. **b** Expected magnetization orientation in the TMR reader depending on the position relative to the coplanar waveguide (CPW). The free layer magnetization changes along the direction of the magnetic field generated by the current in the CPW (I_{CPW}), resulting in a change in TMR. **c** Reader signal (V_{AC}, left axis) and calculated magnetic field in the z-direction (H_z, right axis) during the y-scan at $x = 0$ μm. V_{AC} is normalized by the maximum value during the whole scan in (**d**). A distance of 3 μm is assumed between the HDD head and the CPW for the calculation of H_z. Vertical dashed lines indicate the designed positions of the CPW edges. **d** Color map of the reader signal. The vertical pink line at $x = 0$ corresponds to the scan line in (**c**). **e** Optical microscope image of the CPW. **f** Drawing of the CPW design.

spins from SIL_1 and reflected spins at the SIL_2 interface work to generate the oscillation (precession) of the FGL_1 magnetization. At the same time, STT from the reflected spins at the shield interface, where a higher spin-polarization layer (e.g., FeCo-alloy) is attached[33], induces the oscillation of FGL_2. This simultaneous oscillation of FGL_1 and FGL_2 magnetizations is aimed at forming an antiparallel coupling in the in-plane direction via the dipolar field. The resulting localized microwave magnetic field distribution is particularly suitable for MAMR [4,15].

This STO should also exhibit an alternative mode of operation with negative I_{STO}, where only the FGL_1 magnetization is expected to oscillate due to STT from SIL_1 and SIL_2 (Fig. 1c). In contrast to the positive I_{STO} case, the magnetization reversal occurs in SIL_2. The STT from reflected electrons at the FGL_2 interface does not affect the shield due to the large volume of the shield, and the FGL_1 and shield magnetizations remain in the initial configuration. We note that the change in the coil current polarity reverses the direction and trajectory of the magnetization of all magnetic layers in the STO, thus maintaining the relationship between the I_{STO} polarity and the resulting oscillation mode.

Figure 1e shows the two-terminal STO resistance (R_{STO}) as a function of I_{STO}. The parabolic behavior arises from Joule heating, which is caused by high current density on the order of 10^8 A/cm^2. Additionally, resistance steps appear both on positive and negative I_{STO} at ±1 mA, corresponding to GMR effects due to magnetization reversals of SIL_1 and SIL_2, respectively. Although another resistance step is expected due to FGL_2 magnetization reversal above +5 mA[14], we did not use such a large current in this study to minimize damage in the STO.

Results and discussion

Preparation of the injection-locking measurement

To study the injection locking behavior of STOs to an external microwave, we used a CPW, which generates an Oersted magnetic field from the signal line upon application of a microwave signal. The CPW was fabricated on a sapphire substrate by depositing an electrode film with Ta(10 nm)/Cu(200 nm)/Ta(10 nm)/Au(100 nm), patterning the film into a CPW structure with a 3-μm-wide signal line and a 3-μm gap between the signal line and the ground, and depositing an SiO_2 non-conducting coating layer.

To precisely position the HDD head above the center of the CPW, we used the reader part of the HDD head[30]. The HDD reader utilizes tunneling magnetoresistance (TMR) to detect the vertical magnetic field from magnetic grains on the disk. The TMR reader consists of two magnetic layers separated by an MgO barrier. The magnetization of one magnetic layer is pinned vertically along the z-axis (Fig. 2) via exchange coupling with an antiferromagnetic material (typically IrMn), while the other layer (the free layer) has its magnetization biased along the y-axis. A magnetic field H_z in the $+z$ or $-z$ direction alters the relative magnetization orientation of the two layers, leading to an increase or decrease of TMR, respectively. The width of the TMR reader is less than 20 nm, which is more than two orders of magnitude smaller than the CPW width.

During the positioning, a DC current was applied to the TMR reader, while a low-frequency (1013 Hz) AC current (I_{CPW}) of 9.1 mA was applied to the CPW. The resulting AC voltage (V_{AC}) in the TMR reader, induced by the CPW's Oersted field, was measured using a lock-in amplifier. The relative position between the head and the CPW was scanned using stepping motors (see Methods for sample alignment details).

Figure 2c, d shows the result of the scan. The resistance map (Fig. 2d) clearly reproduces the shape of CPW (Fig. 2e, f). The sign reversal at $y = 0$ μm and the larger amplitude at $x = -50$ to 50 μm are consistent with the magnetic field direction and higher current density in the signal line of the CPW, respectively. The y-direction profile of the reader output was reproduced by simulation assuming a uniform current density in the CPW signal line, a linear response of the TMR sensor to the magnetic field amplitude obtained from Biot–Savart law, and the distance between the HDD head and the CPW of 3 μm (Fig. 2c), where the distance affects the peak and bottom position of H_z in the y-direction (see also Supplementary Fig. 1). In Fig. 2c, we plotted the experimental result and simulated H_z with slightly different zero positions in the vertical axis. The offset appearing in the experiment can be attributed to the contribution from the magnetic field along the y-axis. We used the position $x = y = 0$ μm for the following injection locking measurements.

Spectrum and injection locking experiments

Figure 3a–c shows the setup and the result of conventional spectrum measurements. While applying a DC coil current of 50 mA, we swept I_{STO}. The oscillation of the GMR signal at a frequency of f_{STO} generated by the magnetization oscillation was measured using a spectrum analyzer after separating the DC signals using a bias tee and amplifying the signal by around +50 dB. For these measurements, we used radio frequency (RF) probes with a bandwidth of 50 GHz and directly contacted bare HDD heads extracted from the production process (Fig. 3a) because the original HDD

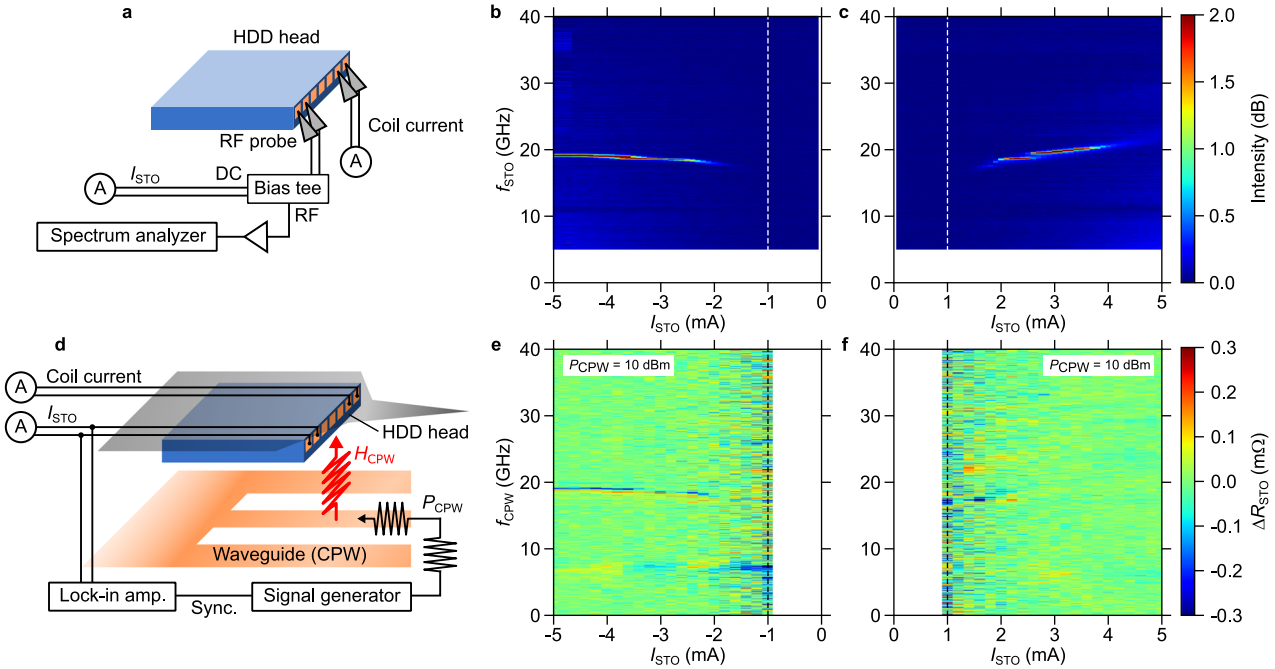

Fig. 3 | Experimental setup and results for spectrum and injection locking measurements. a Setup for spectrum measurement. Radio frequency (RF) probes contact the hard disk drive (HDD) head pads directly. A DC coil current and a spin-torque oscillator (STO) current (I_{STO}) are applied, and the RF signal generated by STO oscillation is separated by the bias tee and measured at a frequency of f_{STO} with the spectrum analyzer after amplification. **b**, **c** Spectrum measurement results with negative and positive I_{STO}, respectively. The intensity is measured from the noise floor. **d** Setup for injection locking measurement. Microwave power (P_{CPW}) with a frequency of f_{CPW} is applied to the coplanar waveguide (CPW), generating a microwave magnetic field (H_{CPW}). The resistance change (ΔR_{STO}) due to injection locking is monitored by the lock-in amplifier connected to the HDD leads, which also supplies the coil current and I_{STO}. **e**, **f** Injection locking measurement results at P_{CPW} = 10 dBm with negative and positive I_{STO}, respectively. The vertical dotted lines in (**b**, **c**, **e**, **f**) indicate I_{STO} values for spin-injection layer flipping (same as Fig. 1e).

leads are incapable of transmitting weak high-frequency signals (see Methods for spectrum measurement details).

Figure 3c shows the spectrum measured with positive I_{STO}. We observed a peak suggesting the coupled oscillation state from f_{STO} = 19 GHz at I_{STO} = +2 mA until 20 GHz at +4 mA. This disappearance of the oscillation at +4 mA is thought to be due to STT imbalance[14]. In the negative I_{STO} case (Fig. 3b), a peak is also observable from I_{STO} = − 2 to −5 mA with a similar frequency to the positive I_{STO} case, which are expected to originate from an isolated FGL_1 oscillation. We note that the signals arising from the difference in oscillation frequencies between FGL and SIL, so-called fictitious peaks, were not detected in our experiments and simulations, in contrast to previous studies[26,27,34]. This may be attributed to the smaller thickness of the SIL in our devices.

Figure 3d–f shows the setup and the results of the injection locking measurement. The production-level HDD head and CPW were aligned as determined previously (Fig. 2). Using a signal generator, we applied high-frequency signals to the CPW set to a power of P_{CPW} and a frequency of f_{CPW}, generating a microwave magnetic field (H_{CPW}) that is injected to the STO. The signal was generated with a 50% duty with a modulation frequency of 1 kHz. A DC coil current of 50 mA and I_{STO} were applied through the HDD leads (Fig. 3d). The resistance difference between the cases with and without H_{CPW} (ΔR_{STO}) was monitored with a lock-in amplifier synchronized with the signal generator at 1 kHz. The 1 kHz signal can be easily measured through the HDD leads (see Methods for injection locking measurement details).

Figure 3e, f shows the dependence of ΔR_{STO} on f_{CPW} mapped as a function of negative and positive I_{STO}, respectively, using the same HDD head as in Fig. 3b, c. On the negative bias side, a clear injection locking signal is observed in which ΔR_{STO} changes from positive to negative as f_{CPW} increases. This signal appears at the same frequency (19–20 GHz) and in the same I_{STO} (−2 to −5 mA) as the signal in Fig. 3b. However, on the positive I_{STO} side, no injection locking signal was detected at the position of the signal observed in Fig. 3c. This absence of a locking signal for positive I_{STO} highlights a clear distinction between the two bias polarities.

Figure 4a–d shows the comparison between the results for spectral measurement and injection locking measurement at I_{STO} = +3.0 and −5.0 mA. In the negative I_{STO} case, the frequency of the peak observed in the spectrum measurement (Fig. 3b) was identical to the center frequency of the injection locking signal (Fig. 4a). In contrast, as shown in Fig. 4b, the injection locking signal is not detectable in the positive I_{STO} case, and only the spectrum peak appeared.

Injection measurement results at other P_{CPW} values are plotted in Fig. 4c, d. At I_{STO} = −5.0 mA, the locking bandwidth increases with increasing P_{CPW} and H_{CPW}, consistent with the previous study[27]. The slope of ΔR_{STO} with respect to f_{CPW} is independent of P_{CPW}, suggesting that ΔR_{STO} originates solely from the locking effect to f_{CPW}, where the relationship between f_{STO} and the oscillation cone angle (the angle between the x-axis and the magnetization) determines ΔR_{STO}. At I_{STO} = +3.0 mA, no injection locking signal was observed even at +15 dBm, further confirming the absence of this effect for positive I_{STO}.

To investigate the absence of injection locking for positive I_{STO} in more detail, we repeated the measurements with P_{CPW} of 15 dBm (Fig. 5) since higher power gives a wider locking range. We found that a locking signal exists within a narrow current range between I_{STO} = +1 mA, where the SIL_1 reversal occurs, and I_{STO} = +2 mA, where the clear spectrum peak was observed in Fig. 3c. Further increasing I_{STO} above +2 mA results in diminished locking signal. This result indicates that even with positive I_{STO}, injection locking can occur after the oscillation appears and before the coupled oscillation becomes stable. After the coupled oscillation becomes stable at +2 mA, the locking signal diminishes because the coupled oscillation is insensitive to injection locking. The locking signals in Fig. 5 mainly consist of negative ΔR_{STO} values in contrast to the symmetric behavior observed in Fig. 4c. This indicates that the locking behavior in the unstable coupled oscillation state with

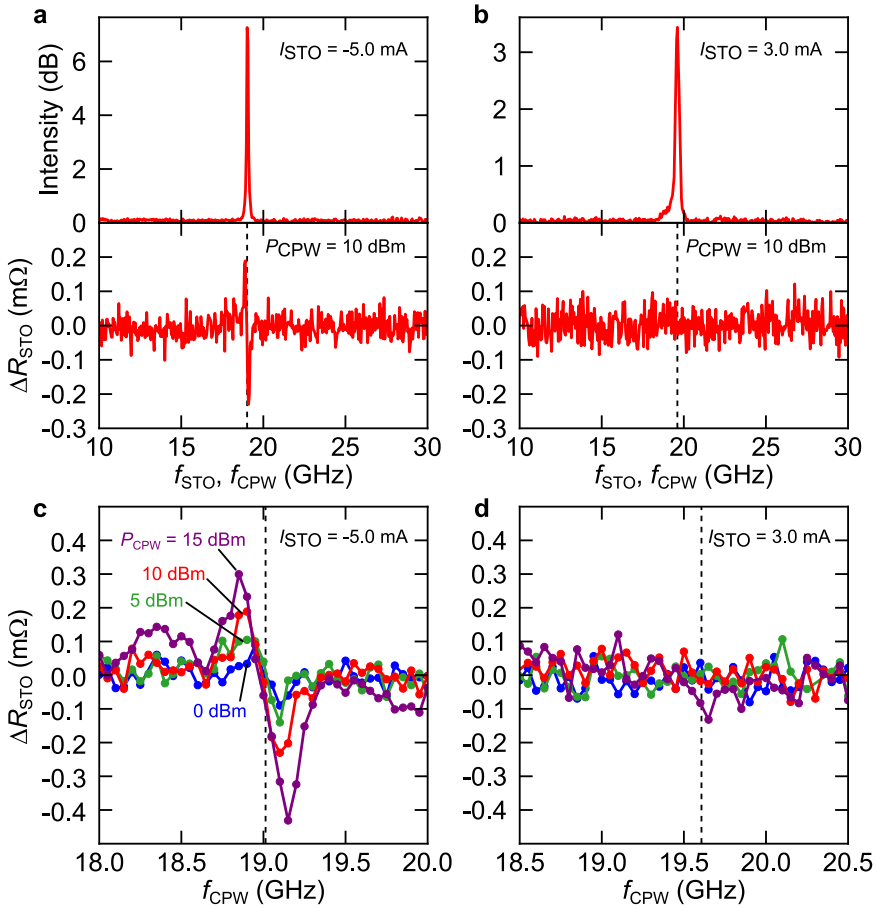

Fig. 4 | Comparisons between spectrum and injection locking measurement results.
a, **b** Spectrum intensity (Top) and resistance change (ΔR_{STO}) due to injection locking for P_{CPW} = 10 dBm (Bottom) as functions of f_{STO} (Top) and f_{CPW} (Bottom) at I_{STO} = −5.0 (**a**) and +3.0 mA (**b**), where P_{CPW}, f_{STO}, f_{CPW} and I_{STO} are the microwave power applied to the coplanar waveguide (CPW), the oscillation frequency of the spin-torque oscillator (STO), the microwave frequency applied to the CPW, and the STO current, respectively.
c, **d** Injection locking result at I_{STO} = −5.0 and +3.0 mA, respectively, with various P_{CPW} (0, 5, 10, 15 dBm). The vertical dashed lines in **a** (Bottom), **b** (Bottom), **c**, and **d** indicate the peak positions in the spectra (**a** (Top) and **b** (Top)).

positive I_{STO} is more complicated than that in the single oscillation state with negative I_{STO}.

Since the injection locking does not occur at a fictitious peak frequency[26], the observed injection locking signal at smaller I_{STO} in Fig. 5 reflects the actual oscillation of FGLs. Therefore, this result supports that the spectrum peaks at larger I_{STO} in Fig. 3c are also related to actual oscillation of FGLs, because the peaks appear continuously at 19 GHz and at I_{STO} = +2 mA (Figs. 3c and 5a) without any anomaly in R_{STO} (Fig. 1e).

Injection locking simulation

For a deeper understanding of the observed injection locking signals, we performed micromagnetic simulations[12,14]. The simulation model includes a part of the pole and shield and whole magnetic layers of the STO, with the same thicknesses as in the experiments. Because H_{gap} is underestimated in this model due to the partial head structure, we added a uniform external DC magnetic field of 0.4 T in the x-direction to align $\mu_0 H_{gap}$ with the reasonable value of 1.5 T. We applied a uniform magnetic field oscillating in the y-direction as H_{CPW}. The magnetization dynamics of each element follows the Landau–Lifshitz–Gilbert (LLG) equation with an STT term[4,35]. Other simulation parameters are listed in Supplementary Table 1.

Figure 6a–d shows the simulated STO spectra as a function of f_{CPW} for I_{STO} = −2.6 and +2.0 mA and for several H_{CPW} values. In the negative I_{STO} case (Fig. 6a, c), f_{STO} was in line with f_{CPW} in the f_{CPW} range from 19.5 to 20.5 GHz and 18 to 22 GHz, respectively. Such frequency alignment accompanied by an increase in the oscillation amplitude and reduction of oscillation linewidth is a typical feature of injection locking[26,27]. The locking bandwidth increases with increasing H_{CPW} (Fig. 6c), consistent with the experimental trend in Fig. 4c.

For comparison with measurements, we evaluated ΔR_{STO} values by calculating the sum of the resistance changes due to the GMR effect at the three interfaces (SIL_1/FGL_1, FGL_1/SIL_2, and FGL_2/shield) and taking its average over 80 ns. The resistance change was defined by -cosθ, where θ is the relative angle between the two magnetization directions across the interface. The simulated ΔR_{STO} exhibited a decrease (increase) at frequencies lower (higher) than the intrinsic f_{STO} and reproduced the experimental result. Additionally, the bottom figure in Fig. 6e shows the averaged phase of FGL_1 magnetization relative to H_{CPW}. The phase also showed positive (negative) shift in the lower (higher) side of f_{CPW} compared to f_{STO}. The phase was zero on average out of the locking regime of f_{CPW} because the magnetization oscillation and H_{CPW} were uncorrelated without locking. We note that the relative phase of the injection locking is different from that of ferromagnetic resonance, where 90 degrees is obtained at the resonant peak.

In contrast to the negative I_{STO} case, no locking behavior was observed in the positive I_{STO} simulations with H_{CPW} = 2.0 mT (Fig. 6b), which corresponds to the same amplitude as in Fig. 6c. However, with a much larger amplitude of 40.0 mT, locking did occur as shown in Fig. 6d, f. The locking range is small considering the large H_{CPW} value of 40.0 mT, and the frequency dependence of ΔR_{STO} is reversed compared to the negative I_{STO} case. In the bottom figure in Fig. 6f, we plotted the phase of the FGL_2 magnetization relative to H_{CPW} at H_{CPW} = 40.0 mT, as well as the phase of FGL_1 for various H_{CPW} values (0.5–40.0 mT) in the positive I_{STO} case. The relative phase was non-zero at the locking center and shows antisymmetric behavior between FGL_1 and FGL_2 magnetizations. Furthermore, the relative phases of FGL1 and FGL2 magnetizations were swapped at some calculation points (f_{CPW} = 19.6 and 20.3 GHz), indicating a more complicated dynamics during the locking as discussed later.

Figure 6g, h is the time-domain plots of the oscillation behavior of the FGLs during injection locking in the negative and positive I_{STO} cases at the center frequency of the locking, 20.4 and 19.9 GHz, respectively. With negative I_{STO}, the FGL_1 oscillation was locked in phase with H_{CPW} (Fig. 6g). FGL_2 magnetization also oscillated slightly in the same phase as H_{CPW}. However, with positive I_{STO}, H_{CPW} lies between FGL_1 and FGL_2 oscillations

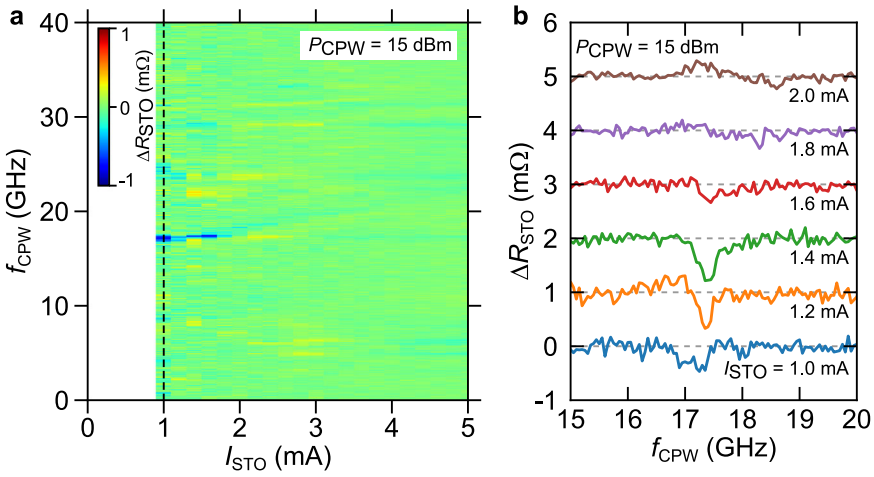

Fig. 5 | Injection locking measurement results with a larger P_{CPW}. a Mapping of resistance change (ΔR_{STO}) due to injection locking at P_{CPW} = 15 dBm with f_{CPW} and positive I_{STO} sweeping, where P_{CPW}, f_{CPW} and I_{STO} are the microwave power applied to the coplanar waveguide (CPW), the microwave frequency applied to the CPW, and the spin-torque oscillator (STO) current, respectively. The vertical dashed line indicates the I_{STO} value for spin-injection layer flipping (same as Fig. 1e). **b** Injection locking result at P_{CPW} = 15 dBm and I_{STO} from 1.0 to 2.0 mA. The plots are shifted vertically by 1 mΩ for clarity.

(Fig. 6h). As summarized in the bottom figures of Fig. 6f, the relative phases were slightly smaller than 90 degrees, indicating that the FGL_1 and FGL_2 magnetizations were canted from the antiparallel configuration.

The simulation results can explain why the coupled state is insensitive to injection locking. As shown in Fig. 6g, when only a single FGL is oscillating (negative I_{STO}), the system can minimize its Zeeman energy by synchronizing its phase with H_{CPW}. Although the STO needs to change its oscillation frequency to align f_{CPW}, the locked state is energetically preferred. However, in the case of coupled oscillation case (positive I_{STO}), there is a trade-off between FGL_1 and FGL_2 in terms of Zeeman energy minimization. Although each FGL prefers to align with H_{CPW}, it is prevented by their antiferromagnetic coupling. Only when H_{CPW} is sufficiently strong can both FGLs approach H_{CPW} symmetrically and form a canted configuration. The order of crossing $m_y = 0$ can be either of FGL_1-H_{CPW}-FGL_2 (Fig. 6h) and FGL_2-H_{CPW}-FGL_1. Because both configurations are stable, the latter configuration was occasionally observed during the simulation (f_{CPW} = 19.6 and 20.3 GHz in Fig. 6f (Bottom)).

Based on the estimated distance of 3 μm between the HDD head and the CPW (Fig. 2c and Supplementary Fig. 1), we can also estimate the H_{CPW} generated for each P_{CPW} in the experiment. Assuming no signal loss in the CPW and RF cables between the CPW and signal generator, the values of $\mu_0 H_{CPW}$ are 0.25, 0.45, 0.80, and 1.42 mT for P_{CPW} = 0, 5, 10, and 15 dBm, respectively. Although there is a difference in the locking range between the experiment (0.3 GHz at P_{CPW} = 15 dBm) and the simulation (2 GHz at $\mu_0 H_{CPW}$ = 1.42 mT), this discrepancy is partly attributable to signal loss in the CPW at frequencies around f_{CPW} = 20 GHz.

We discuss the relationship between the sign of ΔR_{STO} and f_{CPW}. Because the injection locking leads to resistance change at the three interfaces (SIL_1/FGL_1, FGL_1/SIL_2, and FGL_2/shield), the interpretation of ΔR_{STO} is not straightforward. In the negative I_{STO} case, only FGL_1 is oscillating, and the first two interfaces are responsible for the ΔR_{STO} change. Injection locking in STO generally modulates the oscillation cone angle, which increases with higher f_{STO} and f_{CPW} than the original f_{STO} (see Fig. 1e in ref. 27). In the negative I_{STO} with higher f_{STO}, since SIL_1 and SIL_2 are non-flipped and flipped, respectively (Fig. 1c), the angle between SIL_1 and FGL_1 increases, and SIL_2 and FGL_1 decreases at the same time, leading to a cancellation of ΔR_{STO}. Nevertheless, distinct negative ΔR_{STO} signals were observed in higher f_{CPW} sides, and as well as positive ΔR_{STO} signals on the lower f_{CPW} sides (Figs. 4c and 6e), which indicates that the FGL_1/SIL_2 interface is more dominant than the SIL_1/FGL_1 interface. Our simulation results suggest that this asymmetry arises because the out-of-plane component of magnetization is larger in the flipped SIL_2, while the non-flipped SIL_1 has a larger in-plane component and can exhibit oscillation[12]. In the experiment, the non-symmetricity of GMR response, where GMR is more sensitive to changes in the relative magnetization angle around 180 degrees than around 0 degrees[36], may further contribute to this antisymmetric behavior between the SIL_1/FGL_1 and FGL_1/SIL_2 interfaces.

With positive I_{STO} (Fig. 1d), SIL_1 is flipped, and its interface is more influential on ΔR_{STO} than the non-flipped SIL_2 interface. Because the sign of ΔR_{STO} is determined by the flipping, the contribution to ΔR_{STO} from SIL_1/FGL_1 and FGL_1/SIL_2 interfaces leads to the same ΔR_{STO}-f_{CPW} relationship as in the negative I_{STO} case. However, the resistance change at the shield/FGL_2 interface, where the shield magnetization is non-flipped, is added with the same sign as the FGL_1/SIL_2 interface and overcome that at the FGL_1/SIL_2 interface. Therefore, the frequency dependence of ΔR_{STO} is reversed compared to the negative I_{STO} case. However, this reversed behavior is not accessible in the experiment due to limitations on the achievable P_{CPW}.

Finally, we comment on other advanced techniques for analyzing nanoscale magnetization dynamics. As described in the introductory section, superimposing a microwave electrical signal on a bias current is another way to induce injection locking in STOs[3,22–24]. In this type of injection locking, the oscillating STT synchronizes with the magnetization oscillation. However, because multiple spin injections occur at the three interfaces: SIL_1/FGL_1, FGL_1/SIL_2, and FGL_2/shield, the oscillating STT cannot be clearly defined in the dual-FGL STO. Even if oscillation state dependence on sensitivity to current-based injection locking can be observed, the interpretation will be complicated. In contrast, injection locking by microwave magnetic fields ensures that both FGLs experience the same microwave field, allowing for elucidation of their coupling state, as discussed from the viewpoint of Zeeman energy minimization. In addition, microwave electrical signal injection requires high-frequency-compatible lead designs, which are unnecessary for applications like MAMR. On the other hand, the microwave magnetic field can be injected without such design constraints, and injection locking can be detected by measuring ΔR_{STO}.

Recently, combining current-based injection locking with optical detection of magnetization was proposed for analyzing a coupling state of multiple oscillators separated by a few hundred nanometers in the in-plane direction of the thin films[6,37]. While this method offers the advantage of real-space imaging, its spatial resolution limited by the wavelength of light is insufficient for dual-FGL STOs, where the two FGLs are separated by only a few nanometers in the stacking direction of the thin films. Only synchrotron-based x-ray magnetic circular dichroism (XMCD) offers both spatial and temporal resolutions compatible with the size and frequency of STOs[38–40]. Additionally, to combine the microwave field injection with these imaging techniques, a CPW must be placed while keeping the device accessible by light or x-ray, whereas our resistance-based detection can be easily implemented by attaching a CPW to the surface of the devices.

Conclusions

In conclusion, we have developed a method for detecting the coupling state in STOs by utilizing injection locking with an external microwave

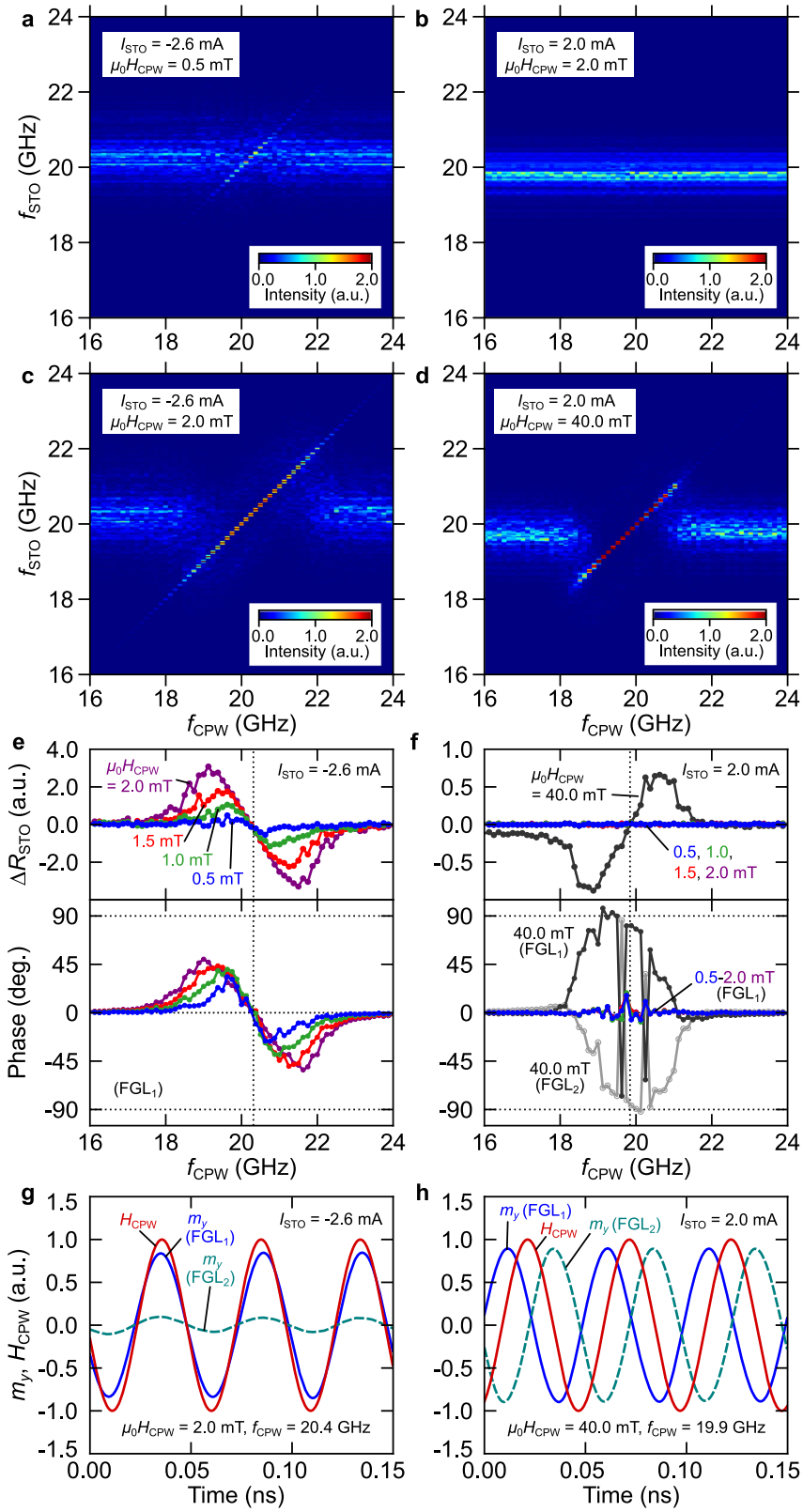

Fig. 6 | Simulation results of injection locking. **a**–**d** Spectrum intensity mapping during injection locking at (I_{STO}, $\mu_0 H_{CPW}$) = (−2.6 mA, 0.5 mT) (**a**), (2.0 mA, 2.0 mT) (**b**), (−2.6 mA, 2.0 mT) (**c**), and (2.0 mA, 40.0 mT) (**d**), where I_{STO} and H_{CPW} is the spin-torque oscillator (STO) current and the microwave magnetic field oscillating in the *y*-direction, respectively. The bottom and vertical axes are the oscillation frequencies of H_{CPW} (f_{CPW}) and the STO (f_{STO}), respectively. **e**, **f** Resistance change (ΔR_{STO}) due to injection locking (Top) and oscillation phase of the first field-generation layer (FGL_1) relative to H_{CPW} (Bottom) during injection locking at I_{STO} = −2.6 (**e**) and +2.0 mA (**f**). Results at $\mu_0 H_{CPW}$ = 0.5–2.0 mT are plotted in both (**e**) and (**f**). The results for $\mu_0 H_{CPW}$ = 40.0 mT and the phase of FGL_2 are added to (**f**). Vertical dotted lines indicate the frequencies used for (**g**) and (**h**). **g**, **h** Time-domain plots of the magnetization in the *y*-direction (m_y) and H_{CPW} at I_{STO} = −2.6 mA (**g**) and +2.0 mA (**h**). f_{CPW} was set to the center of the locking bandwidth for each case. m_y and H_{CPW} were normalized.

magnetic field. We demonstrated this technique on an STO fabricated in a state-of-the-art HDD head. While conventional spectrum measurement cannot differentiate the oscillation states, yielding similar results for different bias polarities, our injection locking measurement clearly distinguished between single, coupled, and unstable coupled oscillation states and confirmed the designed coupled oscillation in the STO, which offers improved oscillation properties and a broader area of applications. Our method utilizes resistance measurement and an external CPW as a microwave field source, eliminating the need for high-frequency output detection or integration of a CPW, which are often incompatible with device structures. Therefore, our method offers a versatile and broadly applicable approach for detecting oscillations and studying coupling effects in both laboratory- and production-level spintronic devices.

Methods

Sample alignment

The CPW was mounted on a 6-axis (x, y, z, θ_x, θ_y, and θ_z) positioner controlled by stepping motors with a resolution of 50 nm in x- and y-directions (Kohzu precision YA07A-R202). First, we roughly aligned the CPW to the HDD head using CCD cameras. For fine positioning, we used a TMR sensor fabricated in the HDD head, as described in the main text. During the scan in the x-y plane, we applied a 1013 Hz sinusoidal voltage to the CPW from a function generator (NF corporation WF1946) and a DC current to the TMR sensor from a DC current source (Keithley 6221) through the HDD leads. A lock-in amplifier (NF corporation LI5640) measured the output voltage.

Spectrum measurement

For the spectrum measurement, we contacted the electrode pads of the HDD head directly, using RF probes applicable up to 50 GHz. I_{STO} and the coil current are supplied by DC current sources (Keithley 6221 and Keysight B2961A, respectively). After separating the RF signals using a bias tee (Keysight 11612B), we amplified the signal using two RF amplifiers (B&Z Technologies BZP140UD1X2 on the bias tee side and Keysight 83050A on the spectrum analyzer side). The total gain was around 50 dB. A resolution bandwidth of 1 MHz was used as a measurement parameter of the spectrum analyzer (Keysight N9030A). We subtracted the noise floor as background, which is the spectra at $I_{STO} = 0$ mA.

Injection locking measurement

After the sample alignment, the DC current sources for I_{STO} and the coil current were connected to the HDD head through the HDD leads. A lock-in amplifier (NF corporation LI5640) is also connected to the I_{STO} line. From a signal generator (Keysight E8257D with a high output power option), RF signals were applied to the CPW with a pulse modulation with a modulation frequency of 1 kHz at a 50% duty cycle. The lock-in amplifier measured the voltage (resistance) difference in the STO between with and without the RF signals, while sweeping the frequency of the RF signals (f_{CPW}) in 0.05 GHz steps at a rate of 0.1 s per point.

Data availability

The related data are available from the corresponding author on reasonable request.

Received: 26 June 2025; Accepted: 15 December 2025;
Published online: 21 January 2026

References

1. Kaka, S. et al. Mutual phase-locking of microwave spin torque nano-oscillators. *Nature* **437**, 389–392 (2005).
2. Mancoff, F. B., Rizzo, N. D., Engel, B. N. & Tehrani, S. Phase-locking in double-point-contact spin-transfer devices. *Nature* **437**, 393–395 (2005).
3. Zahedinejad, M. et al. Two-dimensional mutually synchronized spin Hall nano-oscillator arrays for neuromorphic computing. *Nat. Nanotechnol.* **15**, 47–52 (2020).
4. Takagishi, M. et al. Design concept of MAS effect dominant MAMR head and numerical study. *IEEE Trans. Magn.* **57**, 3300106 (2021).
5. Wu, L. et al. Impact of magnetic coupling and density on STT-MRAM performance. In *2020 Design, Automation & Test in Europe Conference & Exhibition (DATE)*, 1211–1216 (IEEE, 2020).
6. Kumar, A. et al. Spin-wave-mediated mutual synchronization and phase tuning in spin Hall nano-oscillators. *Nat. Phys.* **21**, 245–252 (2025).
7. Grollier, J., Cros, V. & Fert, A. Synchronization of spin-transfer oscillators driven by stimulated microwave currents. *Phys. Rev. B* **73**, 060409(R) (2006).
8. Gusakova, D. et al. Linewidth reduction in a spin-torque nano-oscillator caused by non-conservative current-induced coupling between magnetic layers. *Appl. Phys. Lett.* **99**, 052501 (2011).
9. Kudo, K. et al. Influence of dynamical dipolar coupling on spin-torque-induced excitations in a magnetic tunnel junction nanopillar. *J. Appl. Phys.* **111**, 07C906 (2012).
10. Moriyama, T. et al. Phase locking and frequency doubling in spin-transfer-torque oscillators with two coupled free layers. *Phys. Rev. B* **86**, 060411(R) (2012).
11. Nagasawa, T., Kudo, K., Suto, H., Mizushima, K. & Sato, R. Large-amplitude, narrow-linewidth microwave emission in a dual free-layer MgO spin-torque oscillator. *Appl. Phys. Lett.* **105**, 182406 (2014).
12. Nakagawa, Y., Takagishi, M., Narita, N., Takeo, A. & Maeda, T. Multiple spin injection into coupled field generation layers for low current operation of MAMR heads. *IEEE Trans. Magn.* **58**, 3201005 (2022).
13. Takagishi, M. et al. Microwave assisted magnetic recording: Physics and application to hard disk drives. *J. Magn. Magn. Mater.* **563**, 169859 (2022).
14. Nakagawa, Y. et al. Spin-torque oscillator with coupled out-of-plane oscillation layers for microwave-assisted magnetic recording: Experimental, analytical, and numerical studies. *Appl. Phys. Lett.* **122**, 042403 (2023).
15. Nakagawa, Y. et al. Verification and design of position matching effect in MAMR using dual-FGL STO. *IEEE Trans. Magn.* **60**, 3200106 (2024).
16. Grollier, J., Querlioz, D. & Stiles, M. D. Spintronic nanodevices for bioinspired computing. *Proc. IEEE* **104**, 2024–2039 (2016).
17. Torrejon, J. et al. Neuromorphic computing with nanoscale spintronic oscillators. *Nature* **547**, 428–431 (2017).
18. Kudo, K. & Morie, T. Self-feedback electrically coupled spin-Hall oscillator array for pattern-matching operation. *Appl. Phys. Express* **10**, 043001 (2017).
19. Romera, M. et al. Vowel recognition with four coupled spin-torque nano-oscillators. *Nature* **563**, 230–234 (2018).
20. Kanao, T. et al. Reservoir computing on spin-torque oscillator array. *Phys. Rev. Appl.* **12**, 024052 (2019).
21. Romera, M. et al. Binding events through the mutual synchronization of spintronic nano-neurons. *Nat Commun* **13**, 883 (2022).
22. Rippard, W. H. et al. Injection locking and phase control of spin transfer nano-oscillators. *Phys. Rev. Lett.* **95**, 067203 (2005).
23. Zhou, Y., Persson, J. & Åkerman, J. Intrinsic phase shift between a spin torque oscillator and an alternating current. *J. Appl. Phys.* **101**, 09A510 (2007).
24. Georges, B. et al. Coupling efficiency for phase locking of a spin transfer nano-oscillator to a microwave current. *Phys. Rev. Lett.* **101**, 017201 (2008).
25. Urazhdin, S., Tabor, P., Tiberkevich, V. & Slavin, A. Fractional synchronization of spin-torque nano-oscillators. *Phys. Rev. Lett.* **105**, 104101 (2010).
26. Suto, H. et al. Analysis of an all-in-plane spin-torque oscillator using injection locking to an external microwave magnetic field. *Appl. Phys. Express* **14**, 053001 (2021).
27. Asam, N. et al. Analysis method of a spin-torque oscillator using dc resistance change during injection locking to an external microwave magnetic field. *Appl. Phys. Lett.* **119**, 142405 (2021).
28. Zhu, J.-G., Zhu, X. & Tang, Y. Microwave assisted magnetic recording. *IEEE Trans. Magn.* **44**, 125–131 (2008).
29. Tagawa, I. et al. Advantage of MAMR read-write performance. *IEEE Trans. Magn.* **52**, 3101104 (2016).
30. Jiang, B.-Y., Zhang, K., Machita, T., Chen, W. & Dovek, M. Tunneling magnetoresistive devices as read heads in hard disk drives. *J. Magn. Magn. Mater.* **571**, 170546 (2023).
31. Kent, A. D. & Worledge, D. C. A new spin on magnetic memories. *Nat. Nanotechnol.* **10**, 187–191 (2015).

32. Hu, G. et al. 2X reduction of STT-MRAM switching current using double spin-torque magnetic tunnel junction. In *2021 IEEE International Electron Devices Meeting (IEDM)* 2.5.1-2.5.4 https://doi.org/10.1109/IEDM19574.2021.9720691 (IEEE, 2021).
33. Suto, H. et al. Magnetization dynamics of a flux control device fabricated in the write gap of a hard-disk-drive write head for high-density recording. *J. Appl. Phys.* **129**, 103901 (2021).
34. Zhou, W. et al. Inducing out-of-plane precession of magnetization for microwave-assisted magnetic recording with an oscillating polarizer in a spin-torque oscillator. *Appl. Phys. Lett.* **114**, 172403 (2019).
35. Slonczewski, J. C. Current-driven excitation of magnetic multilayers. *J. Magn. Magn. Mater.* **159**, L1–L7 (1996).
36. Urazhdin, S., Loloee, R. & Pratt, W. P. Noncollinear spin transport in magnetic multilayers. *Phys. Rev. B* **71**, 100401(R) (2005).
37. Alemán, A. et al. Phase and frequency-resolved microscopy of operating spin Hall nano-oscillator arrays. *Nanoscale Horiz* **9**, 1732–1739 (2024).
38. Yu, X. W. et al. Images of a spin-torque-driven magnetic nano-oscillator. *Phys. Rev. Lett.* **106**, 167202 (2011).
39. Bonetti, S. X-ray imaging of spin currents and magnetisation dynamics at the nanoscale. *J. Phys. Condens. Matter* **29**, 133004 (2017).
40. Suto, H. et al. Time-resolved imaging of an operating hard-disk-drive write head using nano-beam x-ray magnetic circular dichroism. *J. Appl. Phys.* **128**, 133903 (2020).

Acknowledgements

The HDD head samples used in this study were fabricated by Headway Technologies, Inc.

Author contributions

Y.N. and H.S. conceived and designed the experiments. Y.N. established the experimental setup, performed measurements, and analyzed the data with the help of H.S. Y.N. performed the micromagnetic simulation. H.S. fabricated the CPW. Y.S. and T.M. supervised the project. All authors discussed the results and wrote the manuscript.

Competing interests

The authors declare no competing interests.

Additional information

Supplementary information The online version contains supplementary material available at https://doi.org/10.1038/s42005-025-02469-4.

Correspondence and requests for materials should be addressed to Yuji Nakagawa.

Peer review information *Communications Physics* thanks Himanshu Fulara, Pranaba Muduli and the other, anonymous, reviewer(s) for their contribution to the peer review of this work. A peer review file is available.